

# Iterative Inference-time Scaling with Adaptive Frequency Steering for Image Super-Resolution

Hexin Zhang<sup>1</sup>, Dong Li<sup>1,✉</sup>, Jie Huang<sup>1</sup>, Bingzhou Wang<sup>1</sup>, Xueyang Fu<sup>1,✉</sup>, Zhengjun Zha<sup>1</sup>

<sup>1</sup>University of Science and Technology of China

zhanghexin@mail.ustc.edu.cn, dongli6@mail.ustc.edu.cn

## Abstract

Diffusion models have become a leading paradigm for image super-resolution (SR), but existing methods struggle to guarantee both the high-frequency perceptual quality and the low-frequency structural fidelity of generated images. Although inference-time scaling can theoretically improve this trade-off by allocating more computation, existing strategies remain suboptimal: reward-driven particle optimization often causes perceptual over-smoothing, while optimal-path search tends to lose structural consistency. To overcome these difficulties, we propose **Iterative Diffusion Inference-Time Scaling with Adaptive Frequency Steering (IAFS)**, a training-free framework that jointly leverages iterative refinement and frequency-aware particle fusion. IAFS addresses the challenge of balancing perceptual quality and structural fidelity by progressively refining the generated image through iterative correction of structural deviations. Simultaneously, it ensures effective frequency fusion by adaptively integrating high-frequency perceptual cues with low-frequency structural information, allowing for a more accurate and balanced reconstruction across different image details. Extensive experiments across multiple diffusion-based SR models show that IAFS effectively resolves the perception-fidelity conflict, yielding consistently improved perceptual detail and structural accuracy, and outperforming existing inference-time scaling methods.

## 1. Introduction

Image super-resolution (SR) aims to recover a high-resolution (HR) image from its low-resolution (LR) counterpart. Previous end-to-end SR models directly learn the mapping process from LR to HR spaces through hand-crafted priors [41, 42] or deep networks [8, 10], producing the super-resolved (SR) images with high structural fidelity but leaving huge improvement space for perceptual quality. More recently, diffusion models (DMs) [16, 30, 31]

✉ Corresponding authors.

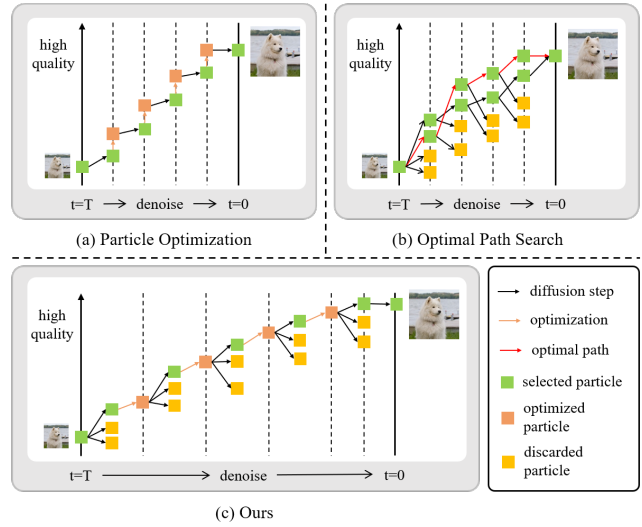


Figure 1. Comparison of different inference-time scaling strategies. (a) Diffusion inference-time scaling based on **Particle Optimization**. (b) Diffusion inference-time scaling based on **Optimal Path Search**. (c) **Iterative Diffusion Inference-time Scaling based on Adaptive Frequency Steering (IAFS)**.

exhibit powerful generative capabilities in modeling data distribution, which are effective in SR tasks that improve the perceptual quality of SR images with vivid fine-grained details [18, 22, 27, 28, 38, 39, 44, 45].

However, diffusion models struggle to balance perceptual quality and structural fidelity in the SR task [2, 28]. Increasing the model’s parameter size or computational budget can push the overall Pareto front of fidelity-perceptual quality towards a better solution domain [20]. Therefore, we hope to use inference-time scaling to increase computational power or iteration in the inference process to improve this problem. But directly applying native inference scaling to super-resolution (SR) is difficult because of image SR tasks differing from text-to-image tasks. On the one hand, the structural conditions of SR are stronger; on the other hand, the improvement in perceptual quality is limited

because of the existing ground-truth images. This means that super-resolution has a higher requirement for balancing low-frequency fidelity and high-frequency perception. However, the core idea of existing inference scaling methods still relies on rewards, which leads to results biased towards reward models, making direct application to SR difficult. On the other hand, optimizing perceptual quality can easily produce illusions and deviate from the true reference image [17]. Therefore, researchers proposed a training-free inference-time scaling technique to overcome this difficulty [9, 12, 14, 19, 23, 24, 29, 34, 47], which improves the generated image quality with limited additional inference computation without changing the model weights.

We reviewed existing inference scaling methods. The mainstream methods that achieve good fidelity and perceptual quality balance can be divided into two categories: one directly optimizes multiple sampled trajectories (particles) at each timestep [12, 14, 24, 47], as shown in Fig. 2 (a); and the other directly finds the optimal path from multiple sampled trajectories generated during the inference process [5, 19, 29], as shown in Fig. 2 (b). However, as can be seen from Tab. 1, the particle optimization method often results in poor perceptual quality of the generated image, while the method of searching for the optimal path results in poor structural fidelity of the generated image. Furthermore, we find that reward models can guide the generation of high-frequency information in images to achieve good perceptual results, but low-frequency structures suffer from defects, while the low-frequency information of different candidate particles is complementary, and their combination helps improve fidelity. Therefore, our goal is to effectively integrate these two components so as to improve the capability of inference scaling to achieve a more favorable balance between fidelity and perceptual quality in SR.

To achieve this target, we propose Iterative Diffusion Inference-Time Scaling with Adaptive Frequency Steering (IAFS), as illustrated in Fig. 2(c). IAFS is built on two principles: iterative refinement and adaptive frequency steering. In SR tasks, high-frequency details are progressively recovered during diffusion, whereas low-frequency structures are largely determined in early steps, as proved in Sec. 3.1. Motivated by this observation, we adopt an iterative strategy that uses the output of each round as pseudo-GT to guide subsequent sampling, and introduce frequency-domain fusion at each timestep to adaptively combine high-frequency perceptual cues with low-frequency structural information. In practice, we first select the best-performing particles at each timestep via a reward function, then decompose them into high-frequency and low-frequency components. The low-frequency part is aligned with similar low-frequency information from the reference particle pool to obtain an adaptive structural representation, which is fused with the high-frequency component to produce the

optimal particle for the next step. During the iteration process, the first iteration uses CLIPIQA [36] to guide sampling, while subsequent iterations adopt a hybrid reward combining CLIPIQA and LPIPS [46] to gradually approach a perceptual-fidelity compromise. Through iterative refinement and frequency fusion, IAFS effectively leverages low-frequency complementarity and high-frequency details across timesteps, yielding high-quality SR results.

The main contributions of this paper are as follows:

- We propose an iterative hybrid reward-guided inference-time scaling method that improves the balance between perceptual quality and structural fidelity in diffusion-based super-resolution. By reformulating inference optimization as a search for optimal frequency information, our approach effectively guides sampling and enhances overall image quality.
- We design an Adaptive Frequency Steering (AFS) method to optimize the iterative sampling process. By aligning and fusing the high-frequency information of the optimal particle with the low-frequency components of high-similarity particles in the pool, AFS yields samples with both high perceptual quality and structural accuracy.
- We conducted extensive experiments to validate our proposed method in conjunction with SR models of different diffusions, demonstrating that our method can significantly improve the perceptual quality and structural fidelity of generated images, and achieve state-of-the-art results for image SR tasks compared with other diffusion inference-time scaling methods.

## 2. Related Works

### 2.1. Diffusion Models for Image Super-Resolution

Early explorations of diffusion models in the field of image super-resolution began with SRDiff [18] and SR3 [28], which generated high-resolution images by training a diffusion model with low-resolution images as conditional inputs. However, this method has a high sampling cost. To address this problem, LDM-SR [27] trains an autoencoder in a low-dimensional latent space and performs a diffusion process, which significantly reduces computational overhead. ResShift [45] reconstructs the forward and reverse Markov chains of traditional diffusion models by introducing a “residual shifting” process between low-resolution (LR) and high-resolution (HR) images, which greatly reduces the difficulty of model estimation. DiffBIR [22] decouples the image restoration process into degradation Removal and information Regeneration, generating high-quality images by introducing a restoration model in the early stages. SeeSR [39] trains a Degradation-Aware Prompt Extractor (DAPE) to generate accurate semantic prompts, which in turn guide a pre-trained T2I model to produce detail-rich and semantically correct results even when handling seman-

tically ambiguous low-resolution images. Despite these advancements, most diffusion-based SR frameworks can not fundamentally address the inference-time limitations that hinder the joint optimization of perceptual quality and structural fidelity.

## 2.2. Inference-Time Scaling for Diffusion Models

Inference-time scaling aims to align pre-trained diffusion models with specific task objectives or quality metrics during generation without requiring additional training [23, 34]. Current methods for the inference sampling process can be divided into particle optimization-based methods and optimal path search-based methods. Particle optimization-based methods guide particles to regions with stronger preferences by imposing constraints on them. Classical Search [47] performs a global search during sampling while using gradients and reward scores to guide samples toward higher-reward local regions. Evolutionary algorithms-based method [14] regards the diffusion model as a black box, optimizing the initial noise in the latent space through genetic algorithms and evolutionary strategies. Optimal path search methods include beam search [11, 19, 25, 32] and SMC (sequential monte carlo)-based [5, 29, 33] methods. Best-of-N (BON) [23, 35] as the simplest path search method, can be regarded as a simplified form of beam search. It achieves optimal path search by simultaneously maintaining  $N$  sampled trajectories and selecting the best output at the last timestep. Diffusion Latent Beam Search (DLBS) [25] first proposed an Inference-time Scaling method based on beam search. At each timestep,  $B$  beams are initialized and  $K$  candidates are generated for each beam. Then, a reward function is used to prune the sampling path. DSearch [19] considers that particles are not easy to evaluate in the first few time steps of the inference process. It proposes a dynamic beam search method, which realizes a dynamic search strategy by gradually increasing the beam width with each timestep. FK-steering method [29] introduces SMC into inference-time scaling and shows that earlier approaches, such as Practical SMC Guidance [5], can be regarded as specific instances of it. The F-SMC method [33] introduces a temperature parameter that varies with the time step to adjust the reward during the FK resampling process.

## 2.3. Inference-time Scaling for Image SR

In order to ensure that the generated images have both high perceptual quality and structural fidelity, inference-time scaling methods that do not require training have been gradually introduced to solve the Image SR problem. Kernel density steering (KDS) [12] as a particle optimization-based method, employs kernel density estimation (KDE) [6, 26] to locate the highest-density region of particle distributions at each inference step, and computes an analytical KDE gradient via mean shift algorithm [4], then uses this gradient to

guide all particles toward a high-density mode. To address the computational challenge of KDE in high-dimensional latent space, KDS introduces a patch-wise mechanism for patch-wise processing. But the method remains computationally expensive even with this design. Moreover, its ensemble-consensus behavior tends to bias toward the distribution mean in SR tasks, resulting in overly smooth reconstructions and degraded perceptual quality because it sacrifices high-frequency texture details for improved low-frequency fidelity. The side-information approach [9] is an optimal path search-based method, which introduces auxiliary information during inference to estimate the expected reward of each particle, pruning suboptimal candidates at every denoising step. By constraining the search space with deterministic cues derived from reference images, it effectively mitigates semantically inconsistent reconstructions. However, this method relies heavily on the availability of side information, requiring auxiliary images similar to the target within the dataset, which greatly limits its applicability. In conclusion, inference-time scaling methods for image SR tasks should combine particle optimization strategy with optimal path search strategy to ensure the diversity of the sampling process and the perceptual-structural quality of the sampling results.

## 3. Methodology

### 3.1. Preliminary

**Reverse Process of Diffusion Models.** The entire process of image generation using DMs is divided into the forward noise-adding stage and the reverse noise-denoising stage. When using pre-trained DMs for image generation, only the reverse denoising process is executed, since the forward process is fixed and implicitly captured by the model training procedure. Let the image corresponding to timestep  $t$  be  $\mathbf{x}_t$ , and the time step corresponding to timestep  $t - 1$  be  $\mathbf{x}_{t-1}$ . Then the conditional probability distribution of  $\mathbf{x}_{t-1}$  is formulated in Eq. 1, and can be equivalently reformulated into the sampling expression shown in Eq. 2.

$$p_{\theta}(\mathbf{x}_{t-1} | \mathbf{x}_t) = \mathcal{N}(\mu_{\theta}(\mathbf{x}_t, t), \sigma_t^2 \mathbf{I}). \quad (1)$$

$$\mathbf{x}_{t-1} = \mu_{\theta}(\mathbf{x}_t, t) + \sigma_t \mathbf{z}, \quad \mathbf{z} \sim \mathcal{N}(0, \mathbf{I}), \quad (2)$$

where  $\mu_{\theta}(\mathbf{x}_t, t)$  is the mean of the corresponding distribution, which is calculated by the pre-trained UNet network, and  $\sigma_t$  is the variance.

**Inference-Time Scaling of Diffusion Models.** Assume the optimal distribution for  $\mathbf{x}_{t-1}$  during the backward reasoning process is  $\mathbf{x}_{t-1}^*$ . From Eq. 2, we know that  $\mu_{\theta}(\mathbf{x}_t, t)$  and  $\sigma_t$  calculated by the pre-trained model are fixed values during inference. Therefore, the process of finding the optimal distribution is the same as the process of finding the optimal noise  $\mathbf{z}^*$ , which can be summarized as finding noise  $\mathbf{z}$

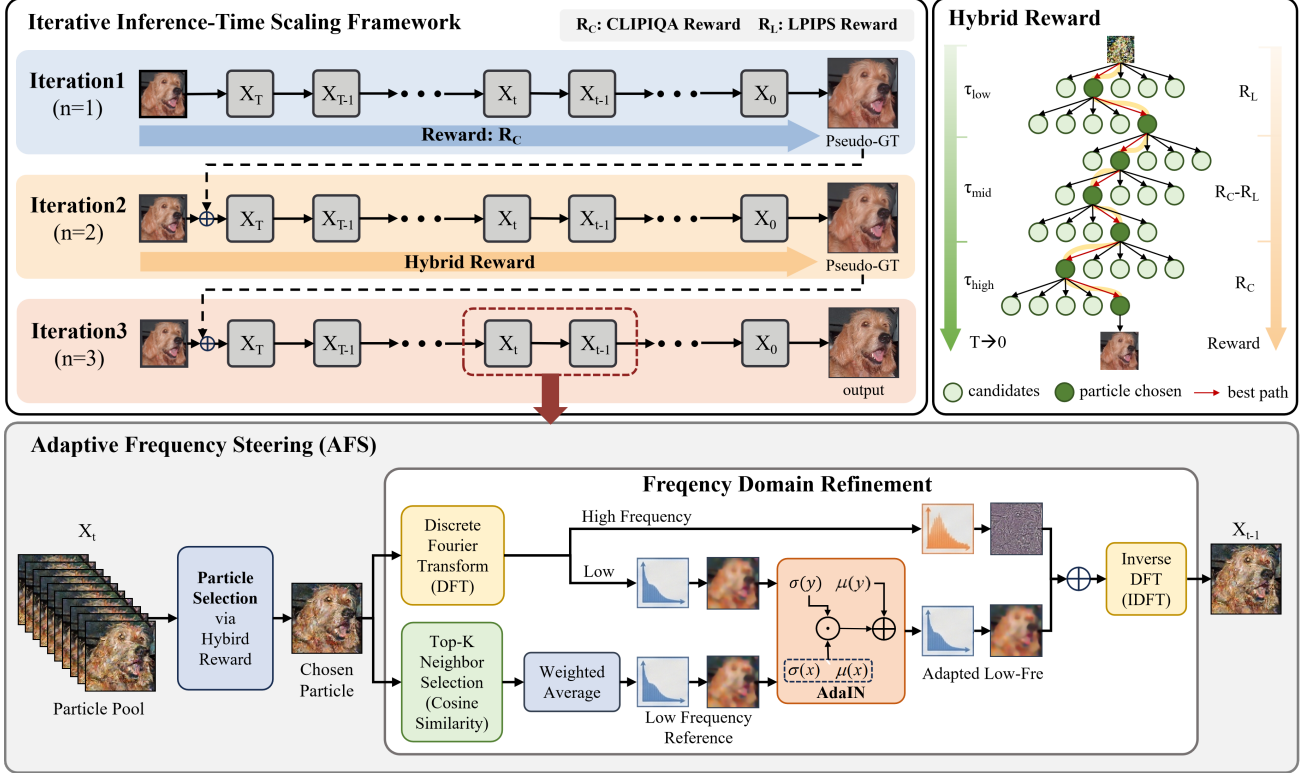


Figure 2. The overall architecture of Iterative Inference-Time Scaling with Adaptive Frequency Steering. At each iteration, the diffusion output serves as pseudo-GT for the next one. For each timestep,  $N$  particles are sampled and the chosen particle is selected via hybrid reward  $R$ . The top- $K$  most similar particles are averaged as the reference. The chosen particle is then decomposed into high/low-frequency components, aligned via Adaptive Instance Normalization (AdaIN), and fused to produce the optimal particle for the next timestep.

that maximizes the expected reward  $R(x)$  of the sample  $x_{t-1}$  from the pre-trained diffusion model  $p_\theta$ , as shown in Eq. 3.

$$z^* = \arg \max_{z \in I} \mathbb{E}_{x \sim p_\theta(x|\psi)} [R(x)]. \quad (3)$$

**Frequency Representation of Reverse Process.** Finding the optimal noise using evaluation methods during the inference process of diffusion is very difficult, but the optimal noise can be obtained through frequency domain decomposition, thereby obtaining the optimal particles. Firstly, we perform a Fourier transform on Eq. 2 to obtain the spectrum corresponding to the distribution of  $x_{t-1}$  as follows:

$$\hat{f}_{x_{t-1}}(\omega) = \exp \left( -i \omega^\top \mu_\theta - \frac{1}{2} \sigma_t^2 \|\omega\|^2 \right) \quad (4)$$

Since  $\mu_\theta(x_t, t)$  and  $\sigma_t$  are fixed values obtained from the pre-trained model at each timestep in the inference process, the first term in Eq. (4) is the phase term, and thus the amplitude spectrum can be expressed as follows:

$$|\hat{f}(\omega)| = e^{-\frac{1}{2} \sigma_t^2 \|\omega\|^2}. \quad (5)$$

In diffusion models, the value of  $\sigma_t$  is relatively large in the early stage of the inference process. Thus,  $\hat{f}(\omega)$  decays rapidly to 0 as  $\omega$  increases and the signal is closer to

pure noise in the spatial domain. In the later stage of the inference process, the value of  $\sigma_t$  decreases, high-frequency information is gradually recovered and more details are restored. Therefore, in the early stage of the inference phase, the optimal particle can be found by evaluating the low-to-mid-frequency information of  $x_{t-1}$ , while in the later stage of the inference phase, the optimal particle can be found by evaluating the high-frequency information of  $x_{t-1}$ .

### 3.2. Iterative Inference-Time Scaling Method

Research shows that the perception metric CLIPIQA [36] is more sensitive to the high-frequency information of images; the CLIPIQA value increases as the high-frequency information of the image becomes more complete [40]. In contrast, the LPIPS [46] metric favors the mid-to-low-frequency structure of images [21]. These complementary frequency sensitivities suggest that CLIPIQA and LPIPS can be jointly utilized as a reward function to guide the diffusion inference process. Following this insight, we assign different roles to the two metrics across the denoising trajectory. In the early stage of the inference phase, LPIPS is used to evaluate the low-frequency information of the particles to find the best particle. In the middle stage of the

---

**Algorithm 1** Iterative Inference-Time Scaling
 

---

**Require:** Diffusion kernel  $p_\theta(x_{t-1} | x_t)$ ; denoiser  $\phi_t$ ;

- 1: iterations  $n$ ; particles  $N$ ;
- 2: frequency segments  $\mathcal{T}_{\text{low}}, \mathcal{T}_{\text{mid}}, \mathcal{T}_{\text{high}}$
- 3: Initialize pseudo reference  $\tilde{y}^{(0)} \leftarrow \emptyset$
- 4: **for**  $i = 1, \dots, n$  **do**
- 5:  $y^{(i)} \leftarrow \begin{cases} \emptyset, & i = 1, \\ \tilde{y}^{(i-1)}, & i > 1 \end{cases}$
- 6: Initialize particles  $x_T^{(k)} \sim \mathcal{N}(0, I), k = 1, \dots, N$
- 7: **for**  $t = T, \dots, 1$  **do**
- 8: Sample  $x_{t-1}^{(k)} \sim p_\theta(x_{t-1} | x_t^{(k)})$  and predict  $\hat{u}_t^{(k)} = \phi_t(x_t^{(k)})$
- 9: Compute rewards  $r_k$  for  $k = 1, \dots, N$  as
 
$$r_k = \begin{cases} R_C(\hat{u}_t^{(k)}), & i = 1, \\ R_L(\hat{u}_t^{(k)}, y^{(i)}), & i > 1, t \in \mathcal{T}_{\text{low}}, \\ R_C(\hat{u}_t^{(k)}) - R_L(\hat{u}_t^{(k)}, y^{(i)}), & i > 1, t \in \mathcal{T}_{\text{mid}}, \\ R_C(\hat{u}_t^{(k)}), & i > 1, t \in \mathcal{T}_{\text{high}}. \end{cases}$$
- 10: Select  $k^* = \arg \max_k r_k$  and apply AFS to refine  $x_t^{(k^*)}$
- 11: **end for**
- 12: Decode  $\hat{x}^{(i)} = \phi_0(x_0^{(k^*)})$  and set  $\tilde{y}^{(i)} \leftarrow \hat{x}^{(i)}$
- 13: **end for**
- 14: **return** final image  $\hat{x}^{(n)}$

---

inference phase, a combination of LPIPS and CLIPQA is used to evaluate the frequency information of the particles. Finally, in the later stage of the inference phase, CLIPQA is used to evaluate the high-frequency information of the particles, ensuring that the best particles can be selected at each timestep. However, using LPIPS throughout the entire inference process is not feasible because LPIPS is a reference-based metric requiring ground-truth images, whereas CLIPQA is a no-reference metric and can reliably filter frequency information even without explicit supervision [40]. To overcome this limitation, we design an iterative hybrid reward-guided strategy. In the first iteration, CLIPQA is used as the reward for particle selection, and the generated result is used as the pseudo-gt for the next iteration. Then particle selection is performed by combining the pseudo-gt with the hybrid reward that changes with the inference process. And this process is repeated  $n$  times, ultimately producing a result that balances both perceptual quality and structural fidelity. The pseudo-code of this process is shown in Algorithm 1.

### 3.3. Adaptive Frequency Steering

Using only rewards to select particles during diffusion inference can lead to an over-preference for reward metrics in

the generated results. This is especially true when selecting an optimal particle and constructing a particle pool at each timestep; if the actual quality of the particle is poor, the entire inference process can collapse. Therefore, it is crucial to optimize and guide the particles during the search process simultaneously. KDS [12] has demonstrated that the particles in the particle pool at each timestep possess "collective intelligence." Based on our analysis of frequencies during the inference process of diffusion, we designed an adaptive frequency steering strategy to optimize the optimal particle as shown in Fig. 2. Let the particle pool at timestep  $t$  be  $\{\mathbf{x}_t^i\}_{i=1}^N$ . Firstly, we use a mixed reward system to select the best particle  $\mathbf{x}_t^*$  as follows:

$$\mathbf{x}_t^* = \arg \max_i R(\mathbf{x}_t^i), \quad (6)$$

Then perform a Discrete Fourier Transform (DFT) on it to obtain the spectrum:

$$\mathcal{F}(\mathbf{x}_t^*) = \mathbf{F}_L^* + \mathbf{F}_H^*, \quad (7)$$

$$\mathbf{F}_L^* = \mathbf{M}_L \odot \mathcal{F}(\mathbf{x}_t^*), \quad \mathbf{F}_H^* = \mathbf{M}_H \odot \mathcal{F}(\mathbf{x}_t^*), \quad (8)$$

where  $\mathbf{M}_L$  and  $\mathbf{M}_H$  are the low-frequency and high-frequency masks. The remaining particles are selected from the top  $K$  similar neighbors based on cosine similarity [41] as follows:

$$\omega_i = \frac{\langle \mathbf{x}_t^i, \mathbf{x}_t^* \rangle}{\|\mathbf{x}_t^i\| \|\mathbf{x}_t^*\|}, \quad \mathcal{N}_K = \text{Top-}K(\omega_i), \quad (9)$$

where  $\omega_i$  represents similarity weight for each particle with  $\mathbf{x}_t^*$ . And then a low-frequency reference is obtained by weighted averaging as follows:

$$\bar{\mathbf{F}}_L = \frac{\sum_{\mathbf{x}_t^{(k)} \in \mathcal{N}_K} \omega_k \mathbf{M}_L \odot \mathcal{F}(\mathbf{x}_t^{(k)})}{\sum_{\mathbf{x}_t^{(k)} \in \mathcal{N}_K} \omega_k}. \quad (10)$$

where  $\bar{\mathbf{F}}_L$  is a low-frequency reference, which aggregates low-frequency commonalities among multiple particles. To ensure style alignment between the master particle and the reference particle, we introduce Adaptive Instance Normalization (AdaIN) [13] to compute an adaptive low-frequency spectrum as follows:

$$\hat{\mathbf{F}}_L = \sigma(\bar{\mathbf{F}}_L) \frac{\mathbf{F}_L^* - \mu(\mathbf{F}_L^*)}{\sigma(\mathbf{F}_L^*)} + \mu(\bar{\mathbf{F}}_L), \quad (11)$$

where  $\mu$  is the mean of channel and  $\sigma$  is variance of channel. Finally, the fused spectrum is obtained by adding the high-frequency component  $\mathbf{F}_H^*$  of the main particle to the adaptive low-frequency spectrum  $\hat{\mathbf{F}}_L$ .

Table 1. Super-Resolution Performance compared with different inference-time scaling methods on ImageNet and DIV2K. The best and second best results are marked in red and blue.

Datasets	ImageNet						DIV2K					
	Method	PSNR	SSIM	LPIPS(↓)	CLIP-IQA	MUSIQ	MANIQA	PSNR	SSIM	LPIPS(↓)	CLIP-IQA	MUSIQ
<b>ResShift</b>	23.01	0.6466	0.2371	0.5860	53.18	0.4191	24.79	0.6273	0.3365	0.5418	59.52	0.4125
+BON	23.31	0.6504	0.2108	0.7038	59.53	0.4938	25.01	<b>0.6305</b>	0.3182	0.6259	63.75	0.4922
+BS	23.38	0.6469	<b>0.2079</b>	<b>0.7823</b>	<b>60.94</b>	<b>0.5026</b>	25.09	0.6281	<b>0.3126</b>	<b>0.6758</b>	<b>64.37</b>	<b>0.5039</b>
+SMC	23.56	0.6557	0.2224	0.6203	56.45	0.4339	25.14	0.6257	0.3285	0.5615	61.49	0.4197
+KDS	23.73	<b>0.6554</b>	0.2379	0.5904	54.30	0.3902	25.21	<b>0.6348</b>	0.3367	0.5502	60.05	0.3955
<b>+IAFS</b>	<b>24.10</b>	0.6458	<b>0.2082</b>	0.7533	59.83	0.4854	<b>25.45</b>	0.6277	<b>0.3119</b>	0.6449	<b>63.92</b>	0.4972
<b>DiffBIR</b>	22.73	0.6189	0.2601	0.6635	65.26	0.5408	23.64	0.5528	0.3629	0.7734	67.31	0.5948
+BON	22.80	0.6201	0.2620	<b>0.7422</b>	66.45	0.5643	23.46	0.5490	0.3511	0.8452	69.14	0.6355
+BS	23.41	0.6190	<b>0.2424</b>	0.6963	<b>67.78</b>	<b>0.5779</b>	23.48	0.5526	<b>0.3492</b>	<b>0.8592</b>	<b>69.97</b>	<b>0.6221</b>
+SMC	23.74	0.6261	0.2530	0.6711	65.64	0.5549	24.38	0.5661	0.3665	0.7829	67.54	0.6083
+KDS	<b>23.85</b>	0.6297	0.2597	0.6658	65.33	0.5254	23.79	0.5658	0.3587	0.7765	67.43	0.5732
<b>+IAFS</b>	23.98	0.6275	<b>0.2403</b>	0.6833	67.89	0.5722	23.86	0.5617	<b>0.3475</b>	0.7969	69.25	0.6204
<b>SeeSR</b>	23.10	0.6258	0.2343	0.6623	64.95	0.5172	23.61	0.5846	0.2983	0.7602	67.78	0.5533
+BON	23.42	0.6331	<b>0.2277</b>	<b>0.7819</b>	68.81	0.5975	23.85	0.5917	0.2956	<b>0.8479</b>	71.35	<b>0.6318</b>
+BS	23.51	0.6267	<b>0.2223</b>	0.7657	<b>69.14</b>	<b>0.6021</b>	24.26	0.5859	<b>0.2887</b>	0.8301	<b>71.64</b>	<b>0.6672</b>
+SMC	23.64	0.6372	0.2305	0.6789	67.93	0.5314	24.63	0.5815	0.2845	0.7723	70.32	0.5749
+KDS	23.81	0.6362	0.2373	0.6678	65.93	0.4922	23.79	0.5933	0.2932	0.7620	68.31	0.5372
<b>+IAFS</b>	<b>23.87</b>	0.6432	<b>0.2175</b>	0.7659	68.10	0.5846	<b>24.91</b>	0.5925	<b>0.2815</b>	0.7836	<b>71.58</b>	<b>0.6277</b>

Table 2. Performance comparison of inference-time scaling methods on RealSR and DRealSR datasets. The best and second best results are marked in red and blue.

Method	RealSR						DRealSR					
	Method	PSNR	SSIM	LPIPS(↓)	CLIP-IQA	MUSIQ	MANIQA	PSNR	SSIM	LPIPS(↓)	CLIP-IQA	MUSIQ
<b>ResShift</b>	0.2860	24.32	0.6230	0.5590	58.69	0.4593	0.3416	26.42	0.6431	0.5248	56.81	0.4423
+BON	0.2853	24.58	0.6353	0.5814	64.78	0.5325	0.3265	26.54	0.6505	0.5800	61.23	<b>0.5058</b>
+BS	<b>0.2785</b>	24.65	0.6370	<b>0.6110</b>	<b>66.15</b>	<b>0.5530</b>	<b>0.3180</b>	26.63	0.6520	<b>0.5937</b>	<b>63.04</b>	<b>0.5257</b>
+SMC	0.2830	24.72	0.6323	0.5782	61.27	0.4991	0.3374	26.68	0.6531	0.5571	58.90	0.4672
+KDS	0.2865	<b>24.86</b>	<b>0.6420</b>	0.5634	59.51	0.4557	0.3389	<b>26.71</b>	<b>0.6555</b>	0.5462	57.79	0.4355
<b>+IAFS</b>	<b>0.2768</b>	<b>24.91</b>	0.6395	0.5920	64.25	0.5231	<b>0.3150</b>	<b>26.75</b>	0.6539	0.5871	61.82	0.4971
<b>DiffBIR</b>	0.3035	24.70	0.6185	0.6178	65.78	0.6221	0.3648	24.57	0.6581	0.6372	64.95	0.6052
+BON	0.3005	24.85	0.6245	0.6472	67.25	0.6441	0.3521	24.72	0.6639	0.6657	67.16	0.6379
+BS	<b>0.2945</b>	25.03	0.6279	<b>0.6623</b>	<b>68.31</b>	<b>0.6572</b>	<b>0.3445</b>	24.80	0.6651	<b>0.6824</b>	<b>68.33</b>	<b>0.6482</b>
+SMC	0.2978	25.10	0.6202	0.6571	66.15	0.6453	0.3501	24.81	0.6575	0.6705	66.27	0.6211
+KDS	0.3010	<b>25.15</b>	<b>0.6331</b>	0.6348	65.82	0.6110	0.3526	24.76	<b>0.6673</b>	0.6520	65.39	0.6035
<b>+IAFS</b>	<b>0.2925</b>	<b>25.21</b>	0.6314	0.6552	67.39	0.6503	<b>0.3417</b>	<b>24.95</b>	0.6671	0.6751	67.94	0.6473
<b>SeeSR</b>	0.2949	25.38	0.6016	0.6612	65.77	0.5882	0.3168	25.27	0.6216	0.6342	65.03	0.5894
+BON	0.2918	25.45	0.6072	0.6874	67.25	0.6175	0.3054	25.39	0.6265	<b>0.6620</b>	67.41	0.6257
+BS	<b>0.2880</b>	25.50	0.6081	<b>0.6923</b>	<b>68.17</b>	<b>0.6359</b>	<b>0.2976</b>	25.44	0.6281	0.6553	<b>68.13</b>	<b>0.6482</b>
+SMC	0.2905	25.58	0.6109	0.6745	66.59	0.6027	0.3037	25.52	0.6305	0.6510	66.29	0.6154
+KDS	0.2940	<b>25.65</b>	<b>0.6148</b>	0.6627	65.25	0.5811	0.3125	<b>25.53</b>	<b>0.6327</b>	0.6489	65.04	0.5855
<b>+IAFS</b>	<b>0.2865</b>	<b>25.70</b>	0.6115	0.6800	67.80	0.6257	<b>0.2956</b>	<b>25.66</b>	0.6310	0.6621	67.50	0.6315

## 4. Experiments

### 4.1. Experiment Setting

We select ImageNet-Test [7, 45] that contains 3,000 images and DIV2K-val [1] as datasets for synthetic image SR evaluation. RealSR [3] and DRealSR [37] are adopted for real-world image SR evaluation. We demonstrate the plug-and-play nature of our algorithms by considering three different baselines: ResShift [45], DiffBIR [22], and SeeSR [39]. For the three baselines, we set their inference timesteps to

15, 50, and 50 during the experiment. To demonstrate the effectiveness of our method, we compared it with Best-of-N (BON) [23], Beam Search (BS) [19], FK-steering (FK) [29], and Kernel Density Steering (KDS) [12]. To ensure the computational budget during inference is equivalent across different methods,  $N$  equal 10 sampling paths are maintained for BON, FK, and KDS during the sampling process, and BS selects the best beam by sampling  $B$  equal 10 beams at each timestep, same as our method. Furthermore, the peripheral reward functions for BON, BS, and FK

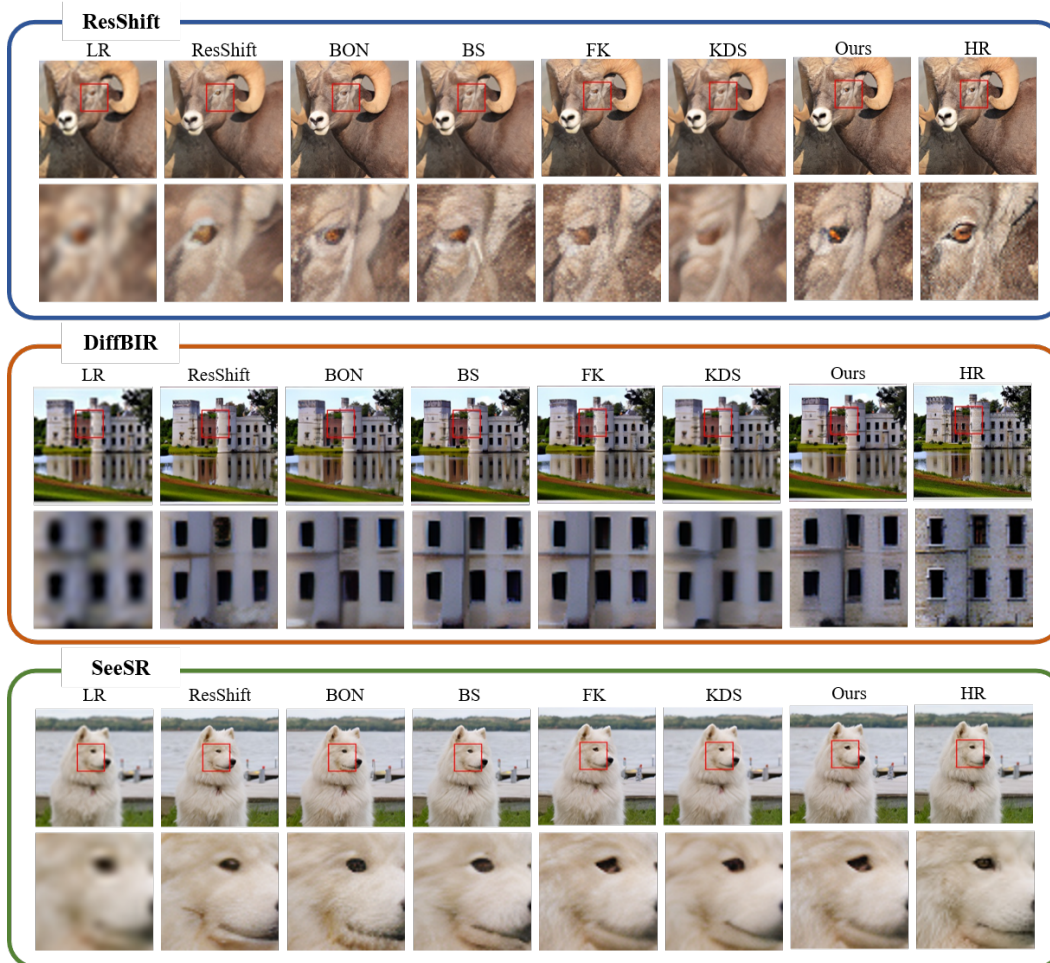


Figure 3. Qualitative comparison of 4× Super-Resolution with different inference-time scaling methods on baselines.

use the same hybrid reward configuration as our method, and we also perform  $n=3$  iterations for each method.

## 4.2. Evaluation on Image Super-Resolution

To evaluate the effectiveness of our method, we compare IAFS against existing inference-time scaling methods across three diffusion SR baselines—ResShift, DiffBIR, and SeeSR. Quantitative comparisons on ImageNet-Test and DIV2K-val are presented in Tab. 1, and results on RealSR and DRealSR are shown in Tab. 2. Across all baselines, IAFS consistently yields substantial improvements over the original models. For each backbone, our method enhances both structural fidelity (PSNR) and structural consistency (SSIM), while simultaneously achieving superior perceptual quality reflected in LPIPS, CLIPQA, MUSIQ, and MANIQA scores. These results demonstrate that IAFS not only strengthens low-frequency structural reconstruction but also recovers richer high-frequency details, thereby achieving a more balanced perceptual–structural

trade-off than the vanilla baselines. When compared with other inference-time scaling strategies, the advantages of IAFS become more explicit. BON and BS introduce only mild guidance during sampling, resulting in limited perceptual improvement and often failing to meaningfully enhance image detail. SMC methods provide stronger particle exploration but still struggle to maintain structural consistency, leading to unstable improvements across metrics. KDS, as a kernel-density-based particle optimization method, tends to bias all trajectories toward similar high-density modes, which improves PSNR/SSIM in some cases but often suppresses high-frequency textures, producing visually smooth yet perceptually degraded outputs. In contrast, IAFS consistently outperforms these methods by simultaneously improving perceptual metrics and maintaining or surpassing structural fidelity, demonstrating clear robustness across different diffusion SR frameworks. Qualitative results in Fig. 3 further validate these findings. Compared with other methods, our approach better restores fine-grained textures,

produces fewer artifacts, and preserves sharper edges while avoiding the perceptual over-enhancement or structural collapse observed in competing methods. Most importantly, IAFS effectively leverages complementary frequency information to avoid the two common failure modes in SR diffusion inference—perceptually strong but structurally inaccurate outputs, and structurally faithful but perceptually dull outputs.

### 4.3. Impact of Hyperparameters

As an iterative guidance strategy, the performance of IAFS is closely related to its key hyperparameters: the number of sampled particles  $N$  and the number of reference particles  $K$  at each timestep as well as the number of iterations  $n$ . We analyze their impact on SR performance (LPIPS, PSNR, SSIM, CLIPIQA, MUSIQ, MANIQA) using the ResShift model on the ImageNet dataset.

**Number of Samples  $N$  and Reference Particles  $K$ .** The number of particles sampled at each timestep ( $N$ ) determines the diversity of sampling paths and directly affects optimal-path selection, while the number of reference particles ( $K$ ) influences the effectiveness of Adaptive Frequency Steering (AFS). As shown in Fig. 4, both perceptual metrics (LPIPS, CLIPIQA) and structural metrics (PSNR, SSIM) exhibit consistent trends as  $N$  and  $K$  vary. Increasing  $N$  from 5 to 10 yields notable gains across all four metrics, but further increasing  $N$  to 20 produces only marginal improvements, indicating saturation relative to the rising computational cost. For  $K$ , the results consistently show that  $K = 2$  outperforms  $K = 3$  and  $K = 4$  in all metrics, while larger  $K$  values provide no additional benefit and often degrade performance. Considering both accuracy and efficiency,  $N = 10$  captures most of the achievable improvement, and  $K = 2$  offers the most reliable frequency guidance. Therefore, the combination  $N = 10$  and  $K = 2$  provides the optimal balance between perceptual quality, structural fidelity, and computation.

**Number of Iterations  $n$ .** The number of iterations plays a crucial role in balancing the perception distortion trade-off and determining computational cost. Tab. 3 shows that iterative refinement improves perceptual metrics such as LPIPS and CLIPIQA in the early stages, with noticeable gains from  $n = 1$  to  $n = 3$ . Beyond the third iteration, the improvement rate diminishes sharply, and by the seventh iteration the perceptual indices essentially reach saturation. A similar trend is observed in structural fidelity: PSNR and SSIM increase steadily during the first few iterations, but their gains plateau as the iteration count continues to rise. Notably, the marginal benefits obtained from iterations beyond  $n = 3$  are minimal. Therefore, considering both efficiency and the perception–structure balance, selecting a moderate iteration count of  $n = 3$  provides the most favorable trade-off, delivering stable improvements on both

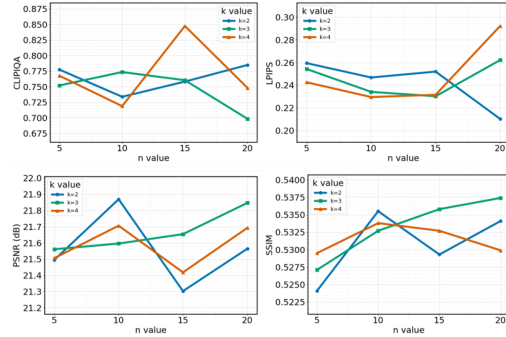


Figure 4. Influence of the number of sampled particles ( $N$ ) and the number of reference particles ( $K$ ) on super-resolution performance. The perceptual metrics (CLIPIQA and LPIPS) and structural metrics (PSNR and SSIM) are plotted against different values of  $N$  under three reference-particle settings ( $K = 2, 3, 4$ ).

Table 3. Performance of IAFS on ResShift across different iterations.

iteration	LPIPS(↓)	PSNR	SSIM	CLIPIQA	MUSIQ	MANIQA
$n = 1$	0.2105	24.05	0.6450	0.7504	59.71	0.4837
$n = 2$	0.2093	24.07	0.6453	0.7527	59.80	0.4841
$n = 3$	0.2082	24.10	0.6458	0.7533	59.83	0.4854
$n = 4$	0.2084	24.09	0.6457	0.7540	<b>59.87</b>	<b>0.4867</b>
$n = 5$	0.2081	24.12	0.6461	0.7539	59.86	0.4860
$n = 6$	0.2080	24.13	0.6462	0.7538	59.85	0.4859
$n = 7$	0.2078	24.17	0.6465	0.7536	59.83	0.4857
$n = 8$	<b>0.2077</b>	<b>24.18</b>	<b>0.6459</b>	0.7541	59.85	0.4861
$n = 9$	<b>0.2077</b>	<b>24.18</b>	0.6457	<b>0.7542</b>	59.86	0.4862
$n = 10$	<b>0.2077</b>	<b>24.18</b>	0.6457	<b>0.7542</b>	59.86	0.4862

perceptual quality and structural fidelity while avoiding redundant computation.

## 5. Conclusion

In this work, we propose an iterative hybrid reward-guided inference-time scaling method with Adaptive Frequency Steering for image super-resolution (SR) tasks, which achieves consistently superior performance compared with existing inference-time scaling methods. During each iteration of sampling, we introduce an adaptive frequency steering (AFS) strategy. The AFS mechanism achieves precise optimization of sampled particles by aligning and fusing low-frequency information of the optimal particle with high-similarity information in the particle pool. Simultaneously, the iterative hybrid reward strategy refines the results through multiple rounds of guidance. Experiments show that our method significantly outperforms existing inference-time scaling techniques in balancing perceptual-structural metrics and generates super-resolution images with both high perceptual quality and high structural fidelity. This addresses the core challenge of balancing perceptual quality and structural fidelity in image SR tasks using diffusion models. We expect our method to be generalized to other image generation tasks in the future.

## References

- [1] Eirikur Agustsson and Radu Timofte. Ntire 2017 challenge on single image super-resolution: Dataset and study. In *Proceedings of the IEEE conference on computer vision and pattern recognition workshops*, pages 126–135, 2017.
- [2] Yochai Blau and Tomer Michaeli. The perception-distortion tradeoff. In *Proceedings of the IEEE conference on computer vision and pattern recognition*, pages 6228–6237, 2018.
- [3] Jianrui Cai, Hui Zeng, Hongwei Yong, Zisheng Cao, and Lei Zhang. Toward real-world single image super-resolution: A new benchmark and a new model. In *Proceedings of the IEEE/CVF international conference on computer vision*, pages 3086–3095, 2019.
- [4] D. Comaniciu and P. Meer. Mean shift: a robust approach toward feature space analysis. *IEEE Transactions on Pattern Analysis and Machine Intelligence*, 24(5):603–619, 2002.
- [5] Meihua Dang, Jiaqi Han, Minkai Xu, Kai Xu, Akash Srivastava, and Stefano Ermon. Inference-time scaling of diffusion language models with particle gibbs sampling. *arXiv preprint arXiv:2507.08390*, 2025.
- [6] Richard A Davis, Keh-Shin Lii, and Dimitris N Politis. Remarks on some nonparametric estimates of a density function. In *Selected Works of Murray Rosenblatt*, pages 95–100. Springer, 2011.
- [7] Jia Deng, Wei Dong, Richard Socher, Li-Jia Li, Kai Li, and Li Fei-Fei. Imagenet: A large-scale hierarchical image database. In *2009 IEEE conference on computer vision and pattern recognition*, pages 248–255. Ieee, 2009.
- [8] Chao Dong, Chen Change Loy, Kaiming He, and Xiaoou Tang. Image super-resolution using deep convolutional networks. *IEEE transactions on pattern analysis and machine intelligence*, 38(2):295–307, 2015.
- [9] Mahdi Farahbakhsh, Vishnu Teja Kunde, Dileep Kalathil, Krishna Narayanan, and Jean-Francois Chamberland. Inference-time search using side information for diffusion-based image reconstruction. *arXiv preprint arXiv:2510.03352*, 2025.
- [10] Daniel Glasner, Shai Bagon, and Michal Irani. Super-resolution from a single image. In *2009 IEEE 12th international conference on computer vision*, pages 349–356. IEEE, 2009.
- [11] Yingqing Guo, Yukang Yang, Hui Yuan, and Mengdi Wang. Training-free guidance beyond differentiability: Scalable path steering with tree search in diffusion and flow models. *arXiv preprint arXiv:2502.11420*, 2025.
- [12] Yuyang Hu, Kangfu Mei, Mojtaba Sahraee-Ardakan, Ulugbek S Kamilov, Peyman Milanfar, and Mauricio Delbracio. Kernel density steering: Inference-time scaling via mode seeking for image restoration. *arXiv preprint arXiv:2507.05604*, 2025.
- [13] Xun Huang and Serge Belongie. Arbitrary style transfer in real-time with adaptive instance normalization. In *Proceedings of the IEEE international conference on computer vision*, pages 1501–1510, 2017.
- [14] Purvish Jajal, Nick John Eliopoulos, Benjamin Shiue-Hal Chou, George K Thiruvathukal, James C Davis, and Yung-Hsiang Lu. Inference-time alignment of diffusion models with evolutionary algorithms. *arXiv preprint arXiv:2506.00299*, 2025.
- [15] Junjie Ke, Qifei Wang, Yilin Wang, Peyman Milanfar, and Feng Yang. Musiq: Multi-scale image quality transformer. In *Proceedings of the IEEE/CVF international conference on computer vision*, pages 5148–5157, 2021.
- [16] Diederik Kingma, Tim Salimans, Ben Poole, and Jonathan Ho. Variational diffusion models. *Advances in neural information processing systems*, 34:21696–21707, 2021.
- [17] Christian Ledig, Lucas Theis, Ferenc Huszár, Jose Caballero, Andrew Cunningham, Alejandro Acosta, Andrew Aitken, Alykhan Tejani, Johannes Totz, Zehan Wang, et al. Photo-realistic single image super-resolution using a generative adversarial network. In *Proceedings of the IEEE conference on computer vision and pattern recognition*, pages 4681–4690, 2017.
- [18] Haoying Li, Yifan Yang, Meng Chang, Shiqi Chen, Huajun Feng, Zhihai Xu, Qi Li, and Yueting Chen. Srdiff: Single image super-resolution with diffusion probabilistic models. *Neurocomputing*, 479:47–59, 2022.
- [19] Xiner Li, Masatoshi Uehara, Xingyu Su, Gabriele Scalia, Tommaso Biancalani, Aviv Regev, Sergey Levine, and Shuiwang Ji. Dynamic search for inference-time alignment in diffusion models. *arXiv preprint arXiv:2503.02039*, 2025.
- [20] Zhengyang Liang, Hao He, Ceyuan Yang, and Bo Dai. Scaling laws for diffusion transformers. *arXiv preprint arXiv:2410.08184*, 2024.
- [21] Xingran Liao, Baoliang Chen, Hanwei Zhu, Shiqi Wang, Mingliang Zhou, and Sam Kwong. Deepwds: Projecting degradations in perceptual space to wasserstein distance in deep feature space. In *Proceedings of the 30th ACM International Conference on Multimedia*, pages 970–978, 2022.
- [22] Xinqi Lin, Jingwen He, Ziyang Chen, Zhaoyang Lyu, Bo Dai, Fanghua Yu, Yu Qiao, Wanli Ouyang, and Chao Dong. Diffbir: Toward blind image restoration with generative diffusion prior. In *European conference on computer vision*, pages 430–448. Springer, 2024.
- [23] Nanye Ma, Shangyuan Tong, Haolin Jia, Hexiang Hu, Yu-Chuan Su, Mingda Zhang, Xuan Yang, Yandong Li, Tommi Jaakkola, Xuhui Jia, et al. Inference-time scaling for diffusion models beyond scaling denoising steps. *arXiv preprint arXiv:2501.09732*, 2025.
- [24] Shunqi Mao, Wei Guo, Chaoyi Zhang, Jieting Long, Ke Xie, and Weidong Cai. Ctrl-z sampling: Diffusion sampling with controlled random zigzag explorations. *arXiv preprint arXiv:2506.20294*, 2025.
- [25] Yuta Oshima, Masahiro Suzuki, Yutaka Matsuo, and Hiroki Furuta. Inference-time text-to-video alignment with diffusion latent beam search. *arXiv preprint arXiv:2501.19252*, 2025.
- [26] Emanuel Parzen. On estimation of a probability density function and mode. *The annals of mathematical statistics*, 33(3): 1065–1076, 1962.
- [27] Robin Rombach, Andreas Blattmann, Dominik Lorenz, Patrick Esser, and Björn Ommer. High-resolution image synthesis with latent diffusion models. In *Proceedings of the IEEE/CVF conference on computer vision and pattern recognition*, pages 10684–10695, 2022.

- [28] Chitwan Saharia, Jonathan Ho, William Chan, Tim Salimans, David J Fleet, and Mohammad Norouzi. Image super-resolution via iterative refinement. *IEEE transactions on pattern analysis and machine intelligence*, 45(4):4713–4726, 2022.
- [29] Raghav Singhal, Zachary Horvitz, Ryan Teehan, Mengye Ren, Zhou Yu, Kathleen McKeown, and Rajesh Ranganath. A general framework for inference-time scaling and steering of diffusion models. *arXiv preprint arXiv:2501.06848*, 2025.
- [30] Jiaming Song, Chenlin Meng, and Stefano Ermon. Denoising diffusion implicit models. *arXiv preprint arXiv:2010.02502*, 2020.
- [31] Yang Song and Stefano Ermon. Generative modeling by estimating gradients of the data distribution. *Advances in neural information processing systems*, 32, 2019.
- [32] Volker Steinbiss, Bach-Hiep Tran, and Hermann Ney. Improvements in beam search. In *ICSLP*, pages 2143–2146, 1994.
- [33] Xun Su, Jianming Huang, Yang Yusen, Zhongxi Fang, and Hiroyuki Kasai. Navigating the exploration-exploitation tradeoff in inference-time scaling of diffusion models. *arXiv preprint arXiv:2508.12361*, 2025.
- [34] Masatoshi Uehara, Yulai Zhao, Chenyu Wang, Xiner Li, Aviv Regev, Sergey Levine, and Tommaso Biancalani. Inference-time alignment in diffusion models with reward-guided generation: Tutorial and review. *arXiv preprint arXiv:2501.09685*, 2025.
- [35] Gabriele Valentini, Eliseo Ferrante, and Marco Dorigo. The best-of-n problem in robot swarms: Formalization, state of the art, and novel perspectives. *Frontiers in Robotics and AI*, 4:9, 2017.
- [36] Jianyi Wang, Kelvin CK Chan, and Chen Change Loy. Exploring clip for assessing the look and feel of images. In *Proceedings of the AAAI conference on artificial intelligence*, pages 2555–2563, 2023.
- [37] Pengxu Wei, Ziwei Xie, Hannan Lu, Zongyuan Zhan, Qixiang Ye, Wangmeng Zuo, and Liang Lin. Component divide-and-conquer for real-world image super-resolution. In *European conference on computer vision*, pages 101–117. Springer, 2020.
- [38] Rongyuan Wu, Lingchen Sun, Zhiyuan Ma, and Lei Zhang. One-step effective diffusion network for real-world image super-resolution. *Advances in Neural Information Processing Systems*, 37:92529–92553, 2024.
- [39] Rongyuan Wu, Tao Yang, Lingchen Sun, Zhengqiang Zhang, Shuai Li, and Lei Zhang. Seers: Towards semantics-aware real-world image super-resolution. In *Proceedings of the IEEE/CVF conference on computer vision and pattern recognition*, pages 25456–25467, 2024.
- [40] Xue Wu, Jingwei Xin, Zhijun Tu, Jie Hu, Jie Li, Nannan Wang, and Xinbo Gao. One-step diffusion-based real-world image super-resolution with visual perception distillation. *arXiv preprint arXiv:2506.02605*, 2025.
- [41] Peipei Xia, Li Zhang, and Fanzhang Li. Learning similarity with cosine similarity ensemble. *Information sciences*, 307: 39–52, 2015.
- [42] Jianchao Yang, John Wright, Thomas S Huang, and Yi Ma. Image super-resolution via sparse representation. *IEEE transactions on image processing*, 19(11):2861–2873, 2010.
- [43] Sidi Yang, Tianhe Wu, Shuwei Shi, Shanshan Lao, Yuan Gong, Mingdeng Cao, Jiahao Wang, and Yujiu Yang. Maniqa: Multi-dimension attention network for no-reference image quality assessment. In *Proceedings of the IEEE/CVF conference on computer vision and pattern recognition*, pages 1191–1200, 2022.
- [44] Tao Yang, Rongyuan Wu, Peiran Ren, Xuansong Xie, and Lei Zhang. Pixel-aware stable diffusion for realistic image super-resolution and personalized stylization. In *European conference on computer vision*, pages 74–91. Springer, 2024.
- [45] Zongsheng Yue, Jianyi Wang, and Chen Change Loy. Resshift: Efficient diffusion model for image super-resolution by residual shifting. *Advances in Neural Information Processing Systems*, 36:13294–13307, 2023.
- [46] Richard Zhang, Phillip Isola, Alexei A Efros, Eli Shechtman, and Oliver Wang. The unreasonable effectiveness of deep features as a perceptual metric. In *Proceedings of the IEEE conference on computer vision and pattern recognition*, pages 586–595, 2018.
- [47] Xiangcheng Zhang, Haowei Lin, Haotian Ye, James Zou, Jianzhu Ma, Yitao Liang, and Yilun Du. Inference-time scaling of diffusion models through classical search. *arXiv preprint arXiv:2505.23614*, 2025.

# Iterative Inference-time Scaling with Adaptive Frequency Steering for Image Super-Resolution

## Supplementary Material

### 6. Theoretical Analysis

In this section, we present a rigorous derivation of Eq. 4 and Eq. 5 from the main text, providing detailed mathematical steps that were omitted for brevity. We also visualize the spectral evolution of the intermediate latent variables across the reverse diffusion process, as shown in Fig. 5. These curves reveal how frequency components are progressively reconstructed from noise to image structure. Leveraging the spectral decay characteristics of Gaussian perturbations, we further establish the theoretical foundation for the proposed Adaptive Frequency Steering (AFS) strategy. Together, these analyses offer a comprehensive understanding of the frequency behavior underlying diffusion inference.

#### 6.1. Justification for Frequency Split

Based on the spectral decay properties of Gaussian noise, we theoretically justify the rationality of the proposed Adaptive Frequency Steering (AFS) strategy. As defined in Eq. 1 of the main text, the reverse denoising process  $p_\theta(\mathbf{x}_t - \mathbf{1} \mid \mathbf{x}_t)$  is modeled as a Gaussian distribution, which is a common formulation in diffusion-based generative models. To analyze the behavior of this process in the frequency domain, we examine the Fourier transform of its probability density function (PDF). This transformation allows us to investigate how uncertainty propagates across different frequency components, which is essential for understanding the selective attenuation or preservation mechanisms that AFS leverages. In probability theory, the Fourier transform of a PDF is referred to as the Characteristic Function, serving as a compact representation that encodes all distributional moments and provides a convenient tool for frequency-domain reasoning. For a  $d$ -dimensional multivariate Gaussian distribution  $X \sim \mathcal{N}(\mu, \Sigma)$ , the probability density function (PDF) is given by:

$$f(x) = \frac{1}{\sqrt{(2\pi)^d |\Sigma|}} \exp\left(-\frac{1}{2}(x - \mu)^\top \Sigma^{-1}(x - \mu)\right). \quad (12)$$

The Fourier transform is defined as  $\hat{f}(\omega) = \mathbb{E}[e^{-i\omega^\top x}]$ . Applying this to the Gaussian distribution yields:

$$\begin{aligned} \hat{f}_{x_{t-1}}(\omega) &= \int_{\mathbb{R}^d} p_\theta(x) e^{-i\omega^\top x} dx \\ &= \exp\left(-i\omega^\top \mu_\theta - \frac{1}{2}\omega^\top \Sigma \omega\right). \end{aligned} \quad (13)$$

In our diffusion setting, the covariance matrix represents isotropic Gaussian noise, where  $\Sigma = \sigma_t^2 I$ . Substituting this

into the equation above yields Eq. 4 from the main text:

$$\hat{f}_{x_{t-1}}(\omega) = \exp\left(-i\omega^\top \mu_\theta - \frac{1}{2}\sigma_t^2 \|\omega\|^2\right). \quad (14)$$

To analyze the energy distribution across frequencies, we focus on the Magnitude Spectrum. Utilizing the property of complex moduli  $|e^{i\theta}| = 1$ , the magnitude of the phase term  $\exp(-i\omega^\top \mu_\theta)$  is unity. Consequently, the amplitude spectrum is determined by the real exponential component:

$$\begin{aligned} |\hat{f}(\omega)| &= |\exp(-i\omega^\top \mu_\theta)| \cdot \left| \exp\left(-\frac{1}{2}\sigma_t^2 \|\omega\|^2\right) \right| \\ &= 1 \cdot \exp\left(-\frac{1}{2}\sigma_t^2 \|\omega\|^2\right) \\ &= \exp\left(-\frac{1}{2}\sigma_t^2 \|\omega\|^2\right). \end{aligned} \quad (15)$$

This confirms Eq. 5 in the main text.

#### 6.2. Frequency Evolution in Inference Process

We compute the Radially Averaged Power Spectral Density (RAPSD) for the sampled trajectories. Specifically, we sample Gaussian noise  $x_T$  and perform the reverse denoising steps using the pre-trained ResShift backbone. For each timestep  $t$ , we apply a 2D Discrete Fourier Transform (DFT) to  $x_t$ , compute the magnitude spectrum, and then perform azimuthal integration to obtain the 1D PSD profile. Fig. 5 illustrates the evolution of the 1D PSD curves from  $t = 14$  (initial noise state) to  $t = 0$  (final generated image). The X-axis represents spatial frequency (radius), and the Y-axis represents the power magnitude in a logarithmic scale. The empirical analysis of spectral evolution reveals a clear temporal disparity in feature reconstruction. Low-frequency components rapidly converge to the target distribution, establishing the global structure during the early stages of inference. In contrast, high-frequency components exhibit prolonged energy fluctuations, with fine-grained details recovering only in the final steps. These observations provide a solid physical interpretation for the proposed Adaptive Frequency Steering (AFS) strategy: the early-stage stability of low-frequency information justifies its use as Pseudo-GT for structural guidance, whereas the delayed recovery of high-frequency textures necessitates an iterative refinement mechanism. Together, these properties enable AFS to effectively balance structural fidelity and perceptual quality.

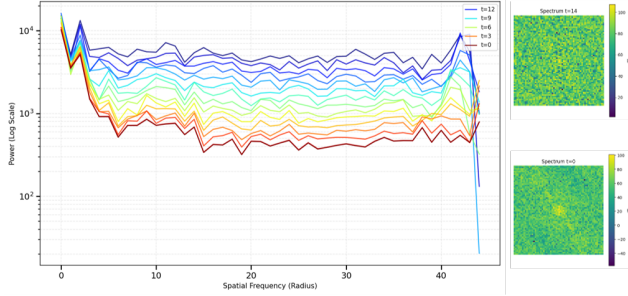


Figure 5. Evolution of the 1D Power Spectral Density (PSD) during the reverse diffusion process.

## 7. Implementation Details

In this section, we present supplementary derivations and clarifications that support the formulations introduced in the main paper. We first provide additional details on the frequency decoupling mechanism within the AFS framework. In addition, we supplement and compare different reward scheduling strategies in the particle optimization process.

### 7.1. Spatial Frequency Decomposition

In Sec. 2 of the main text, we formulated the Adaptive Frequency Steering (AFS) mechanism using Discrete Fourier Transform (DFT) and spectral masking (Eq. 7, Eq. 8) to provide a clear theoretical motivation for frequency separation. However, in practical deployment, direct ideal low-pass filtering in the frequency domain often introduces undesirable Gibbs phenomena in the spatial domain. Therefore, we adopt Spatial Gaussian Filtering as an efficient and robust approximation of frequency-domain low-pass filtering in our implementation. By the convolution theorem, spatial convolution with a Gaussian kernel is equivalent to element-wise multiplication with a Gaussian function in the frequency domain. This approach not only achieves a "soft" frequency split that avoids ringing artifacts but also effectively preserves the spatial continuity of features. Specifically, given the latent variable  $x_t$  at timestep  $t$ , we extract the low-frequency component  $x_{\text{low}}$  and the high-frequency component  $x_{\text{high}}$  as follows:

$$x_{\text{low}} = \mathcal{G}(x_t; k, \sigma), \quad x_{\text{high}} = x_t - x_{\text{low}}, \quad (16)$$

where  $\mathcal{G}(\cdot)$  denotes a Gaussian blur operator. Based on empirical tuning, we set the kernel size to  $k = 9$  and the standard deviation to  $\sigma = 1.0$ . This configuration effectively suppresses high-frequency noise while preserving essential structural information, thereby providing a stable foundation for subsequent AdaIN-based alignment.

### 7.2. Hybrid Reward Scheduling

This section details the reward-scheduling strategy employed during the iterative refinement process ( $n > 1$ ). In

iterative refinement, each subsequent iteration builds upon the predictions of the previous one, making the design of the reward schedule crucial for achieving a stable and progressively improving optimization trajectory. We conducted experiments using the ResShift baseline on the ImageNet [7] dataset, with the ResShift [45] inference time step set to 15. This setting ensures a consistent evaluation protocol across different reward configurations, allowing us to isolate the influence of reward scheduling itself. Once a pseudo-GT is obtained from the initial iteration, the primary objective shifts to balancing the preservation of structural fidelity with the continuous enhancement of perceptual quality. To identify the optimal integration strategy for these conflicting objectives, we investigated four distinct reward scheduling configurations. Let  $\mathcal{R}_C$  denote the perceptual reward (CLIPQA [36]) and  $\mathcal{R}_L$  denote the structural penalty (LPIPS [46]). We evaluated the following settings:

- LPIPS-Only:** The guidance relies solely on minimizing the perceptual distance to the pseudo-GT throughout the entire reverse process ( $r = -\mathcal{R}_L$ ).
- Constant Hybrid:** A fixed weighted combination of perception and structure is applied at every timestep ( $r = \mathcal{R}_C - \mathcal{R}_L$ ).
- Linear Scheduling:** The weight of the perceptual term linearly increases while the structural term decreases as  $t \rightarrow 0$ , promoting structure early and texture late ( $r = \alpha_t \mathcal{R}_C - (1 - \alpha_t) \mathcal{R}_L$ ).
- Segmented Scheduling:** A staged approach where the inference process is divided into three phases: structural alignment, transitional fusion, and perceptual refinement.

As presented in Tab. 4, the experimental result reveals that the LPIPS-only strategy exhibits a clear phenomenon of reward hacking. While it achieves the lowest LPIPS score (0.1976), this metric over-optimization comes at a severe cost to other dimensions. It yields the lowest PSNR (23.24 dB) and SSIM (0.6435), indicating that enforcing strict feature-space constraints throughout the entire inference process overly restricts the generative diversity, preventing the model from hallucinating necessary high-frequency details (evidenced by the lowest CLIPQA score of 0.7106). The CLIPQA-LPIPS and Linear strategies, which incorporate perceptual guidance earlier or continuously, tend to bias the generation towards visual pleasantness at the expense of fidelity. Although they achieve superior CLIPQA scores (0.7539 for Constant), their structural metrics (PSNR/SSIM) are notably suppressed compared to segmented method. In contrast, the segmented strategy maintains competitive perceptual performance without succumbing to the artifacts associated with reward hacking or structural degradation. This confirms that decoupling structural and perceptual guidance into separate temporal windows is essential for generating photorealistic images that remain

faithful to the input.

Table 4. Performance of different reward scheduling strategies.

Reward Schedule	PSNR	SSIM	LPIPS( $\downarrow$ )	CLIQQA	MUSIQ	MANIQA
LPIPS	23.24	0.6435	<b>0.1976</b>	0.7106	61.44	0.5190
CLIQQA-LPIPS	23.73	0.6475	0.2043	<b>0.7539</b>	60.68	0.5195
Linear	23.73	0.6466	0.2042	0.7368	60.26	<b>0.5313</b>
Segmented	<b>24.13</b>	<b>0.6485</b>	0.2089	0.7312	<b>61.02</b>	0.5075

## 8. Additional Ablation Studies

In this section, we provide a comprehensive analysis of the core design choices within our IAFS framework. We first investigate the impact of different perceptual metrics when serving as the guidance reward during the initial iteration. Subsequently, we conduct a fine-grained search to identify the optimal temporal thresholds for our segmented scheduling strategy.

### 8.1. Ablation on Perception Reward

The quality of the pseudo-ground truth (pseudo-GT) generated in the first iteration ( $n = 1$ ) is pivotal for the stability of subsequent refinements. Since this initial step relies solely on a non-reference perceptual reward, the choice of the metric directly influences the initial structural foundation. To determine the most effective guidance signal, we evaluated three state-of-the-art non-reference image quality assessment (IQA) metrics as the optimization objective: CLIP-IQA, MUSIQ [15], and MANIQA [43]. The quantitative results are summarized in Tab. 5, we can observe that MUSIQ and MANIQA achieve the highest scores on their respective metrics (67.76 for MUSIQ and 0.6049 for MANIQA). However, this comes at a significant cost to structural fidelity and general perceptual quality. Specifically, using MANIQA results in a PSNR drop of nearly 1 dB (23.10 dB vs. 24.05 dB) and a degradation in LPIPS compared to CLIPIQA. These findings indicate that while specialized IQA metrics like MUSIQ and MANIQA are effective for evaluation, CLIPIQA offers better generalization and alignment with both perception and structural consistency when used as an optimization objective. Consequently, we adopt CLIPIQA as the default perceptual reward to ensure a high-quality starting point for the iterative refinement process.

Table 5. Performance of different perceptual rewards in the first iteration.

Reward	LPIPS( $\downarrow$ )	PSNR	SSIM	CLIQQA	MUSIQ	MANIQA
CLIQQA	<b>0.2105</b>	<b>24.05</b>	0.6450	<b>0.7504</b>	59.71	0.4837
MUSIQ	0.2134	23.29	<b>0.6464</b>	0.7158	<b>67.76</b>	0.5385
MANIQA	0.2124	23.10	0.6418	0.7035	60.97	<b>0.6049</b>

### 8.2. Ablation on Transition Thresholds

To further optimize the Segmented Scheduling strategy, we conducted an ablation study on the specific time thresholds that define the three phases. We specifically analyze two key hyperparameters: the start timestep for introducing CLIPIQA ( $\tau_{\text{clipiqa}}$ ) and the end timestep for removing LPIPS ( $\tau_{\text{lpiqs}}$ ). The segmented reward scheduling strategy is shown in Fig. 6.

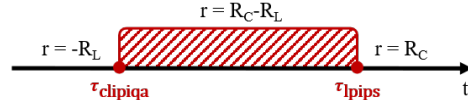


Figure 6. The segmented reward scheduling strategy with  $\tau_{\text{clipiqa}}$  and  $\tau_{\text{lpiqs}}$ .

We evaluated multiple combinations of  $[\tau_{\text{clipiqa}}, \tau_{\text{lpiqs}}]$  on a randomly sampled subset of 1,000 images from the ImageNet validation set using the ResShift backbone ( $T = 15$ ). The quantitative results are comprehensively summarized in Tab. 7. Comparing the sub-tables where  $\tau_{\text{clipiqa}}$  ranges from 0 to 9, we observe a distinct trade-off. When  $\tau_{\text{clipiqa}}$  is small (e.g.,  $\tau_{\text{clipiqa}} \in [0, 2]$ ), meaning perceptual guidance is introduced very late in the denoising process, the model achieves high structural fidelity (SSIM  $\approx 0.652$ ) but suboptimal perceptual quality. This indicates that intervening only in the final few steps is insufficient to hallucinate vivid high-frequency details. Conversely, setting  $\tau_{\text{clipiqa}}$  too high (e.g.,  $\tau_{\text{clipiqa}} \geq 8$ ) introduces perceptual gradients while the image is still heavily corrupted by noise. For a fixed  $\tau_{\text{clipiqa}}$ , varying  $\tau_{\text{lpiqs}}$  controls the duration of the mixed guidance phase. The results show that retaining the LPIPS constraint for too long prevents the model from generating sharp textures, as evidenced by lower MANIQA and MUSIQ scores. However, removing it too early causes the generation to drift away from the pseudo-GT, harming fidelity. By analyzing the Pareto frontier of structural fidelity (PSNR/SSIM) and perceptual quality (LPIPS/CLIQQA), we identify the configuration  $[\tau_{\text{clipiqa}} = 4, \tau_{\text{lpiqs}} = 7]$  as the optimal operating point. Under this setting, the model achieves a PSNR of 24.13 dB and an SSIM of 0.6485, which are among the highest across all combinations. Simultaneously, it maintains excellent perceptual performance with an LPIPS of 0.2089 and a competitive CLIPIQA score. This specific schedule effectively utilizes the mid-inference stage ( $t \in [4, 7]$ ) to transition from structural correction to texture refinement, ensuring a robust balance between faithfulness and realism. Consequently, we adopt  $[\tau_{\text{clipiqa}} = 4, \tau_{\text{lpiqs}} = 7]$  as the default setting for all subsequent experiments.

Table 6. Comparison of time and memory under different methods in the first iteration and the next iteration.

Method	BON		BS		FK		KDS		Ours	
	n=1	n=2								
Time (s)	5.002s	5.020s	47.17s	55.58s	49.49s	53.11s	131.7s	131.7s	50.10s	58.62s
Memory (Gb)	6.00Gb	6.00Gb	6.00Gb	6.00Gb	6.00Gb	6.00Gb	3.87Gb	3.87Gb	6.00Gb	6.00Gb

## 9. Runtime & Computational Complexity

To assess the feasibility of IAFS in practical deployment scenarios, we conducted a systematic computational cost analysis, benchmarking our proposed method against existing inference-time scaling techniques. This section first outlines the experimental setup and testing protocols, followed by a quantitative comparison of runtime latency and peak GPU memory usage across different strategies.

### 9.1. Experimental Setup

All performance benchmarks were conducted in a unified hardware environment featuring a single NVIDIA GeForce RTX 4090 GPU (24GB VRAM) paired with an Intel Xeon Gold 6248 CPU, implemented using the PyTorch 2.1 framework with CUDA 12.1 acceleration. To ensure reliable measurements, we recorded the average inference time for generating a single  $256 \times 256$  resolution image and the peak GPU memory usage, with all reported results averaged over 50 consecutive runs following a warm-up phase to eliminate initialization jitter.

### 9.2. Comparative Analysis

Tab. 6 details the computational costs and performance metrics for each method on the ImageNet dataset using the ResShift backbone, where comparative methods (BON [23], BS [19], FK [29], KDS [12]) adopt  $N = 10$  candidate particles and employ CLIPIQA as the first-iteration reward with the same segmented scheduling in the next iteration. As shown, BON achieves the lowest latency due to its simple parallel sampling, whereas KDS incurs the highest cost because of expensive kernel density optimization, making it impractical for real-time use. Our IAFS strikes a balanced trade-off, and its frequency decomposition and adaptive steering introduce only modest overhead, reflected by the small time increase from  $n = 1$  to  $n = 2$ . Memory usage remains around 6.00 GB for most search-based methods, indicating that storage of high-dimensional latent variables constitutes the primary bottleneck. Overall, IAFS demonstrates deployment-friendly efficiency, offering strong frequency-aware guidance within standard memory budgets and avoiding the extreme latency of optimization-heavy baselines, with future improvements potentially achievable via adaptive particle pruning to enhance real-time applicability.

## 10. More Qualitative Results

To further substantiate the robustness of our proposed IAFS framework, we provide an extended qualitative comparison on real-world images. We integrate various inference-time scaling strategies—specifically Best-of- $N$  (BON), Beam Search (BS), FK-Steering (FK), and Kernel Density Steering (KDS)—into the ResShift backbone and evaluate their performance against our method. Fig. 7 presents visual results across diverse scenarios, including architectural structures, text, animal fur, and human faces. While search-based strategies like BON, BS, and FK generally improve sharpness compared to the vanilla ResShift baseline, they often introduce semantic artifacts or lose structural fidelity. KDS relies on kernel density estimation to guide particles toward high-density regions, tends to sacrifice high-frequency texture for stability. These visual comparisons align with our quantitative findings, confirming that the adaptive frequency steering mechanism allows the model to selectively enhance high-frequency details while strictly adhering to the low-frequency structural constraints, thereby generating super-resolved images that are both visually pleasing and faithful to the input. The result further demonstrate that IAFS maintains consistent performance across diverse real-world distributions, highlighting its robustness and practical applicability.

## 11. Potential Limitations

While the proposed Iterative Diffusion Inference-Time Scaling with Adaptive Frequency Steering (IAFS) effectively mitigates the inherent conflict between perceptual enhancement and structural fidelity in super-resolution, the method still presents notable limitations. The primary bottleneck originates from the computational overhead introduced during inference. Specifically, IAFS requires sampling a pool of  $N$  particles per timestep and executing  $n$  refinement iterations to progressively adjust and stabilize the frequency components. As a result, the overall inference time increases approximately linearly with respect to both  $N$  and  $n$ . Despite this limitation, the added computation is justified in applications demanding high-frequency consistency, fine-grained textures, and robust structural preservation, where IAFS demonstrably reduces over-smoothing and suppresses structural hallucination compared to existing approaches.

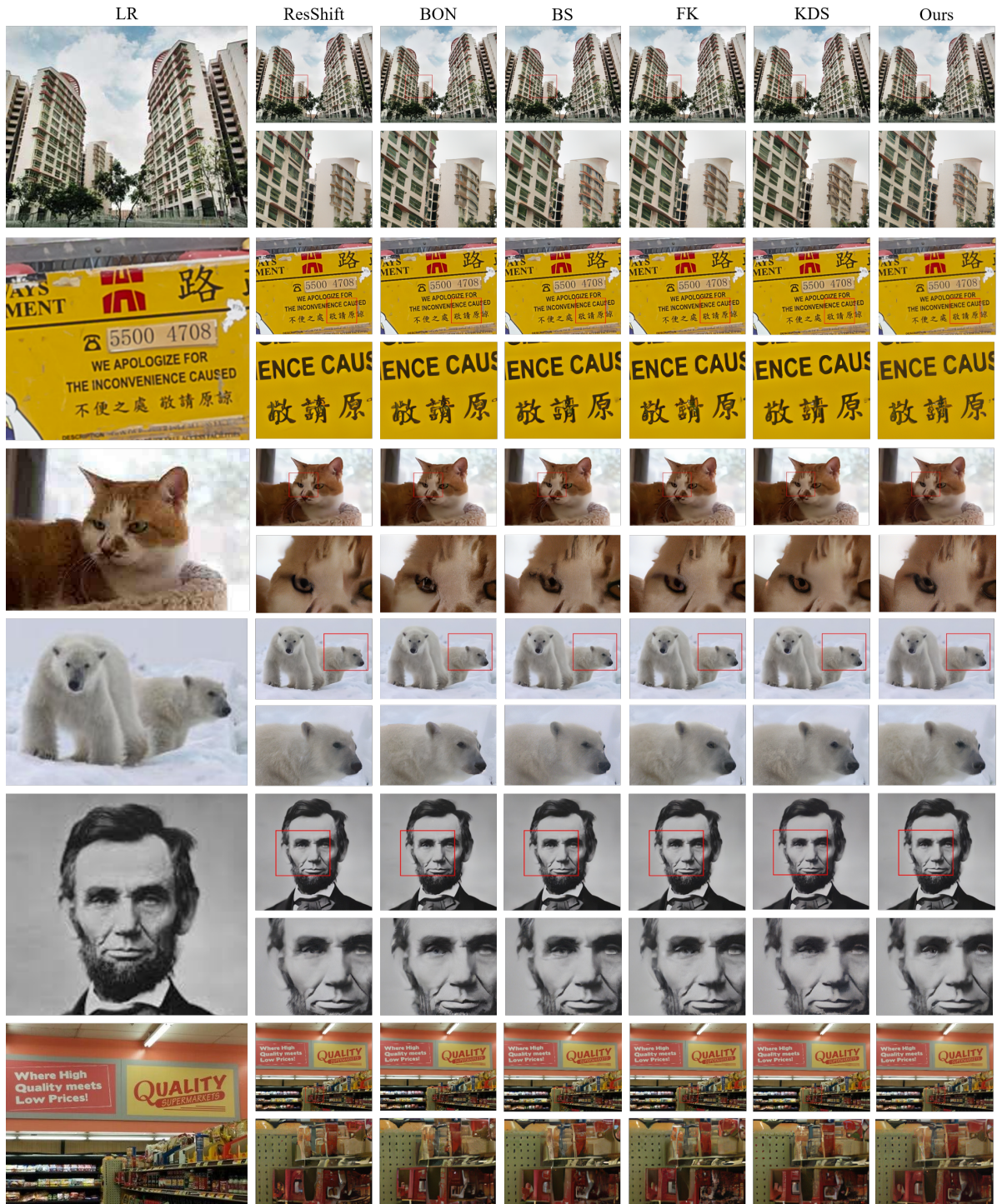


Figure 7. Extended qualitative comparison on real-world images.

Table 7. Quantitative Comparison of Different Combinations of  $[\tau_{\text{clipiqa}}, \tau_{\text{pips}}]$ . The best and second best results are marked in red and blue.

$\tau_{\text{pips}}$	$\tau_{\text{clipiqa}} = 0$						$\tau_{\text{pips}}$	$\tau_{\text{clipiqa}} = 1$					
	PSNR	SSIM	LPIPS( $\downarrow$ )	CLIQQA	MUSIQ	MANIQA		PSNR	SSIM	LPIPS( $\downarrow$ )	CLIQQA	MUSIQ	MANIQA
1	24.05	0.6493	0.2056	<b>0.7679</b>	<b>64.49</b>	0.5004	1	24.15	0.6523	0.2128	0.7699	59.16	0.4828
2	24.05	<b>0.6498</b>	0.2051	<b>0.7602</b>	60.44	0.4983	2	24.15	0.6523	0.2128	0.7699	59.16	0.4828
3	24.05	0.6495	0.2047	0.7388	60.65	<b>0.5012</b>	3	24.15	0.6522	0.2123	0.7699	58.99	0.4791
4	<b>24.09</b>	<b>0.6497</b>	0.2075	0.7243	60.65	0.4897	4	24.15	<b>0.6525</b>	0.2135	0.7690	58.95	0.4761
5	<b>24.06</b>	0.6492	0.2058	0.7203	60.58	0.4908	5	24.15	<b>0.6526</b>	0.2132	0.7694	59.03	0.4777
6	24.05	0.6485	0.2054	0.7265	60.92	0.4912	6	<b>24.18</b>	0.6518	0.2114	0.7683	59.13	0.4842
7	24.04	0.6492	0.2045	0.7252	<b>61.11</b>	0.4944	7	<b>24.16</b>	0.6520	<b>0.2110</b>	0.7689	59.26	<b>0.4849</b>
8	24.05	0.6486	0.2037	0.7269	60.32	0.4967	8	24.15	0.6520	<b>0.2109</b>	0.7718	59.33	0.4840
9	24.04	0.6477	0.2018	0.6976	60.56	0.4873	9	24.14	0.6516	0.2113	0.7735	<b>59.45</b>	<b>0.4879</b>
10	24.02	0.6459	0.2018	0.7326	60.53	<b>0.5069</b>	10	24.11	0.6513	0.2118	0.7727	<b>59.50</b>	0.4837
11	23.93	0.6461	<b>0.2012</b>	0.7234	60.26	0.4973	11	24.11	0.6512	0.2125	<b>0.7753</b>	59.19	0.4829
12	23.95	0.6449	<b>0.1994</b>	0.7182	59.64	0.4991	12	24.11	0.6511	0.2130	<b>0.7760</b>	59.08	0.4805
$\tau_{\text{pips}}$	$\tau_{\text{clipiqa}} = 2$						$\tau_{\text{pips}}$	$\tau_{\text{clipiqa}} = 3$					
	PSNR	SSIM	LPIPS( $\downarrow$ )	CLIQQA	MUSIQ	MANIQA		PSNR	SSIM	LPIPS( $\downarrow$ )	CLIQQA	MUSIQ	MANIQA
2	24.15	0.6522	0.2124	0.7416	59.18	0.4782	2	24.16	0.6524	0.2141	0.7300	58.79	0.4756
3	24.14	0.6521	0.2129	0.7417	59.09	0.4760	3	24.16	0.6524	0.2141	0.7300	58.79	0.4756
4	24.14	<b>0.6525</b>	0.2130	0.7433	59.19	0.4740	4	<b>24.19</b>	<b>0.6529</b>	0.2144	0.7302	58.86	0.4740
5	<b>24.18</b>	<b>0.6526</b>	0.2126	0.7501	59.34	0.4767	5	<b>24.18</b>	<b>0.6531</b>	0.2141	0.7276	59.06	0.4709
6	<b>24.16</b>	0.6519	0.2107	0.7495	59.45	0.4822	6	24.17	0.6525	0.2122	0.7277	59.09	0.4770
7	24.15	0.6521	<b>0.2101</b>	0.7535	59.49	<b>0.4839</b>	7	24.16	0.6522	<b>0.2115</b>	0.7299	<b>59.14</b>	<b>0.4803</b>
8	24.14	0.6519	<b>0.2103</b>	0.7559	59.56	<b>0.4839</b>	8	24.13	0.6520	<b>0.2120</b>	0.7311	<b>59.19</b>	0.4802
9	24.11	0.6515	0.2105	0.7609	<b>59.60</b>	<b>0.4858</b>	9	24.12	0.6515	0.2123	0.7398	58.99	<b>0.4820</b>
10	24.11	0.6512	0.2111	0.7609	<b>59.62</b>	0.4819	10	24.12	0.6512	0.2130	0.7384	59.02	0.4796
11	24.11	0.6512	0.2119	<b>0.7630</b>	59.41	0.4798	11	24.12	0.6509	0.2135	<b>0.7438</b>	58.76	0.4779
12	24.11	0.6511	0.2123	<b>0.7639</b>	59.31	0.4790	12	24.13	0.6510	0.2140	<b>0.7433</b>	58.57	0.4771
$\tau_{\text{pips}}$	$\tau_{\text{clipiqa}} = 4$						$\tau_{\text{pips}}$	$\tau_{\text{clipiqa}} = 5$					
	PSNR	SSIM	LPIPS( $\downarrow$ )	CLIQQA	MUSIQ	MANIQA		PSNR	SSIM	LPIPS( $\downarrow$ )	CLIQQA	MUSIQ	MANIQA
4	<b>24.13</b>	<b>0.6493</b>	0.2108	0.7284	60.27	0.5034	4	<b>24.19</b>	<b>0.6542</b>	0.2125	0.7152	59.06	<b>0.4694</b>
5	<b>24.12</b>	0.6488	0.2099	0.7273	60.42	0.5019	5	<b>24.19</b>	0.6538	0.2110	0.7151	<b>59.10</b>	<b>0.4701</b>
6	<b>24.12</b>	<b>0.6490</b>	0.2098	0.7267	60.82	0.5041	6	<b>24.19</b>	0.6538	0.2110	0.7151	<b>59.10</b>	<b>0.4701</b>
7	<b>24.13</b>	0.6485	0.2089	0.7312	61.02	0.5075	7	24.20	<b>0.6540</b>	<b>0.2095</b>	0.7198	<b>59.16</b>	0.4668
8	24.10	0.6481	0.2079	0.7321	<b>62.29</b>	0.5066	8	<b>24.20</b>	0.6539	<b>0.2100</b>	0.7185	59.08	0.4655
9	24.08	0.6485	0.2049	<b>0.7327</b>	62.10	<b>0.5142</b>	9	24.18	0.6536	0.2108	0.7180	58.95	0.4648
10	24.03	0.6477	<b>0.2040</b>	<b>0.7324</b>	<b>62.14</b>	<b>0.5126</b>	10	24.17	0.6534	0.2112	0.7141	58.79	0.4645
11	24.05	0.6484	<b>0.2046</b>	0.7320	62.12	0.5123	11	24.16	0.6528	0.2117	<b>0.7192</b>	58.48	0.4613
12	24.06	0.6485	0.2051	0.7320	61.33	0.5014	12	24.16	0.6528	0.2118	<b>0.7191</b>	58.68	0.4622
$\tau_{\text{pips}}$	$\tau_{\text{clipiqa}} = 6$						$\tau_{\text{pips}}$	$\tau_{\text{clipiqa}} = 7$					
	PSNR	SSIM	LPIPS( $\downarrow$ )	CLIQQA	MUSIQ	MANIQA		PSNR	SSIM	LPIPS( $\downarrow$ )	CLIQQA	MUSIQ	MANIQA
6	24.18	0.6549	0.2108	<b>0.6946</b>	<b>58.96</b>	0.4621	6	24.23	<b>0.6563</b>	<b>0.2102</b>	0.6651	58.15	<b>0.4595</b>
7	<b>24.19</b>	<b>0.6557</b>	<b>0.2095</b>	0.6931	58.85	<b>0.4697</b>	7	<b>24.23</b>	<b>0.6560</b>	<b>0.2097</b>	0.6659	58.24	0.4535
8	<b>24.20</b>	<b>0.6556</b>	<b>0.2106</b>	<b>0.6982</b>	58.85	0.4625	8	<b>24.23</b>	<b>0.6560</b>	<b>0.2097</b>	0.6659	58.24	0.4535
9	24.18	0.6550	0.2111	0.6928	58.92	0.4653	9	<b>24.19</b>	0.6555	0.2103	0.6667	58.31	<b>0.4597</b>
10	24.17	0.6549	0.2117	0.6914	58.73	<b>0.4668</b>	10	<b>24.19</b>	0.6552	0.2110	0.6664	58.25	0.4562
11	24.18	0.6553	0.2116	0.6911	58.57	0.4591	11	24.17	0.6551	0.2115	<b>0.6668</b>	<b>58.41</b>	0.4541
12	<b>24.20</b>	0.6552	0.2118	0.6912	<b>58.94</b>	0.4604	12	<b>24.19</b>	0.6549	0.2116	<b>0.6681</b>	<b>58.95</b>	0.4569
$\tau_{\text{pips}}$	$\tau_{\text{clipiqa}} = 8$						$\tau_{\text{pips}}$	$\tau_{\text{clipiqa}} = 9$					
	PSNR	SSIM	LPIPS( $\downarrow$ )	CLIQQA	MUSIQ	MANIQA		PSNR	SSIM	LPIPS( $\downarrow$ )	CLIQQA	MUSIQ	MANIQA
8	<b>24.05</b>	<b>0.6474</b>	0.2059	0.7215	59.60	0.5002	8	24.25	<b>0.6542</b>	<b>0.2087</b>	<b>0.6482</b>	<b>58.37</b>	<b>0.4564</b>
9	24.04	0.6470	0.2037	0.7216	60.72	<b>0.5066</b>	9	<b>24.25</b>	<b>0.6544</b>	0.2092	0.6474	58.20	0.4506
10	24.03	0.6464	<b>0.2026</b>	0.7256	<b>61.06</b>	0.5062	10	<b>24.25</b>	<b>0.6544</b>	0.2092	0.6474	58.20	0.4506
11	24.03	0.6466	0.2026	<b>0.7313</b>	<b>61.15</b>	<b>0.5067</b>	11	24.21	0.6536	0.2097	<b>0.6481</b>	58.23	<b>0.4577</b>
12	24.02	<b>0.6478</b>	<b>0.2023</b>	<b>0.7377</b>	60.89	0.5049	12	24.22	0.6538	0.2092	0.6477	58.07	0.4554